Cell Membrane Orientation Visualized by Polarized Total Internal Reflection Fluorescence

Susan E. Sund,* Joel A. Swanson,# and Daniel Axelrod*
*Biophysics Research Division and Department of Physics, and #Department of Microbiology and Immunology, University of Michigan, Ann Arbor, Michigan 48109 USA

ABSTRACT In living cells, variations in membrane orientation occur both in easily imaged large-scale morphological features, and also in less visualizable submicroscopic regions of activity such as endocytosis, exocytosis, and cell surface ruffling. A fluorescence microscopic method is introduced here to visualize such regions. The method is based on fluorescence of an oriented membrane probe excited by a polarized evanescent field created by total internal reflection (TIR) illumination. The fluorescent carbocyanine dye diI-C_{18}-(3) (diI) has previously been shown to embed in the lipid bilayer of cell membranes with its transition dipoles oriented nearly in the plane of the membrane. The membrane-embedded diI near the cell-substrate interface can be fluorescently excited by evanescent field light polarized either perpendicular or parallel to the plane of the substrate coverslip. The excitation efficiency from each polarization depends on the membrane orientation, and thus the ratio of the observed fluorescence excited by these two polarizations vividly shows regions of microscopic and submicroscopic curvature of the membrane, and also gives information regarding the fraction of unoriented diI in the membrane. Both a theoretical background and experimental verification of the technique is presented for samples of 1) oriented diI in model lipid bilayer membranes, erythrocytes, and macrophages; and 2) randomly oriented fluorophores in rhodamine-labeled serum albumin adsorbed to glass, in rhodamine dextran solution, and in rhodamine dextran-loaded macrophages. Sequential digital images of the polarized TIR fluorescence ratios show spatially-resolved time-course maps of membrane orientations on diI-labeled macrophages from which low visibility membrane structures can be identified and quantified. To sharpen and contrast-enhance the TIR images, we deconvoluted them with an experimentally measured point spread function. Image deconvolution is especially effective and fast in our application because fluorescence in TIR emanates from a single focal plane.

INTRODUCTION

Several biologically interesting phenomena involve local variations in membrane orientation on a distance scale near or less than the microscope resolution limit. Examples include: 1) exocytosis and endocytosis, which involves microscopic or submicroscopic blebbing or invagination; 2) vesicular fusion, in which vesicles are adherent or in close proximity to exofacial or cytofacial surfaces of the plasma membrane; and 3) cell surface ruffling of plasma membranes in response to various stimuli.

Existing optical microscope techniques can image such features with varying levels of clarity. Phase-based imaging often cannot show these features because of their small size or small variations in refractive index. Standard epi-illumination (EPI) fluorescence microscopy may show such membrane irregularities as a variation in brightness of an incorporated membrane probe. However, that intensity variation can be a result of several factors that cannot be distinguished from each other, including local variations in: fluorophore concentration or quantum efficiency; the effective amount of membrane due to bunching, adherent vesicles, and tangential viewing; contributions from out-of-focus planes; and orientation of the membrane.

We present here a method for directly viewing the last factor—membrane orientation—distinctly from the other factors in cell/substrate contact regions. This allows visualization of micromorphological structures that otherwise cannot be seen clearly. The method uses the unique electric polarization properties of an evanescent field created by total internal reflection (TIR) at the substrate–cell medium interface, in combination with labeling by an oriented membrane probe such as 1,1′-dihexadecyl-3,3,3′,3′-tetramethylindocarbocyanine [diI-C_{16}-(3), or diI]. The principle of the new polarized TIR fluorescence technique (p-TIRF) is explained here, and examples are presented on lipid bilayers, red cells, and living macrophages. (Recently, evanescent polarization has been used to observe orientations of single molecules in plastic films: see Dickson et al., 1998).

The images can be made particularly sharp by use of two-dimensional (2D) image deconvolution. This deconvolution is especially effective and simple for TIR images because they contain almost no intensity contributions from out-of-focus planes.

Received for publication 6 January 1999 and in final form 7 June 1999.
Address reprint requests to Dr. Daniel Axelrod, Biophysics Research Division, University of Michigan, Ann Arbor, MI 48109. Tel.: 734-764-5280; Fax: 734-764-3323; E-mail: daxelrod@umich.edu.

0006-3495/99/10/2266/18 $2.00

THEORY

Qualitative theory

In TIR, light incident upon a dielectric interface at a supercritical angle from the high refractive index side creates an

oscillatory evanescent field in the lower refractive index medium that exponentially decays perpendicular to the interface and propagates in the direction along the interface. Typically, in a TIRF-modified microscope, the dielectric interface is the interface between the cells and the substrate plane upon which the cells adhere. The p-TIRF technique exploits the fact that incident light polarized in the plane of incidence creates an evanescent field that is predominately polarized normal to the interface (Fig. 1, *top*); the advantage of this polarization is discussed below. By contrast, in a standard EPI illumination fluorescence microscope, the excitation light propagates normal to that interface and thereby is polarized parallel to the interface.

Polarized EPI fluorescence of diI in artificial lipid vesicles (Bradley et al., 1973) and in red cell ghosts (Axelrod, 1979) show that the great majority of diI molecules incorporate into the lipid bilayer with transition dipoles pointing nearly in the plane of the bilayer. Figure 2 shows a schematic cross section of a diI-labeled membrane containing regions that are parallel (substrate-parallel) and nonparallel (oblique) to the substrate. The oblique region could represent, for example, membrane curvature from ruffling, endo- or exocytosis, vesicle prefusion, or formation of apoptotic bodies. Throughout this paper, the z axis is defined to be normal to the coverslip and the x axis is parallel to the coverslip in the plane of incidence. As seen in Fig. 2, z-polarized (z-pol) light barely excites diI in substrate-parallel regions, but preferentially excites diI in oblique regions. Conversely, x-polarized (x-pol) and y-polarized (y-pol) light most effectively excites diI in substrate-parallel regions and less effectively in oblique regions (dependent upon the azimuthal angle of the local membrane orientation).

Comparison of images made by excitation with different polarizations provides information about membrane orien-

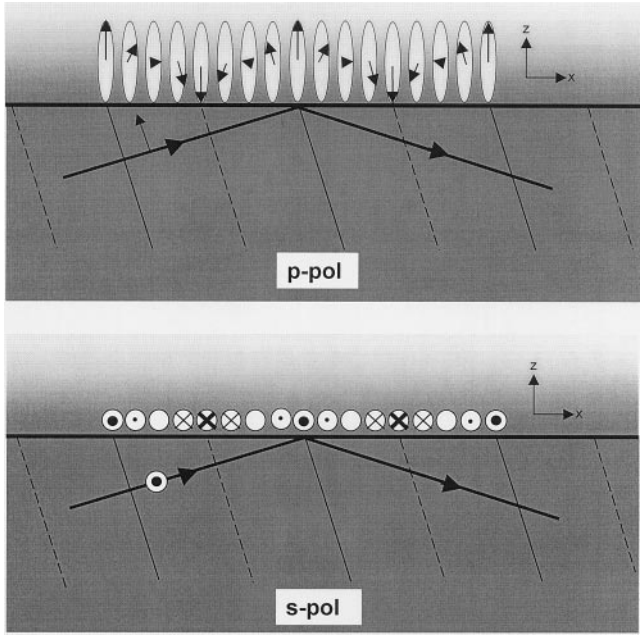

FIGURE 1 Schematic drawing of the evanescent polarization resulting from p-pol (in the plane of incidence) and s-pol (normal to the plane of incidence) incident light. The incident light wavefronts (with the intervals from solid to dashed wavefront lines representing one-half of a wavelength in the glass) define the spacing of the spatial period along the interface, and reflected wavefronts are not shown. The p-pol evanescent field is elliptically polarized in the x–z plane (primarily z-pol with a weaker x-component at a relative phase of $\pi/2$), and the s-pol evanescent field is completely y-pol. In the s-pol drawing, a circle with a dot or $\times$ in the middle represents a polarization vector pointing perpendicularly outward or inward to the plane of the paper, respectively. For pictorial clarity, only two periods of evanescent electric field oscillation are shown; in reality, the evanescent region is much more extended and contains many more periods of oscillation in the x-direction. The exact phase relationship between the incident field and the evanescent field is a function of incidence angle and is not represented here.

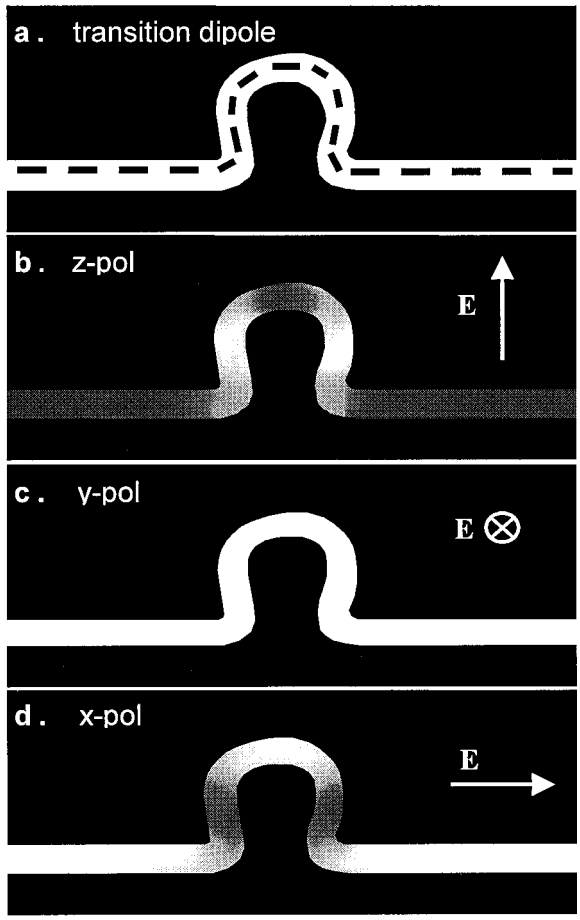

FIGURE 2 Schematic drawing of the excitation probability of oriented fluorophores embedded in a membrane in x-, y-, and z-pol evanescent fields. The TIRF substrate is assumed to be horizontal, and the membrane is depicted in cross section with a curved region corresponding to a bleb or an invagination. (*a*) The direction of absorption dipole μ (*dashes*), here assumed to be parallel to, and free to rotate in, the local plane of the membrane. (*b*), (*c*), (*d*) The excitation probability pattern upon illumination with an electric field **E** polarized in the z, y, and x direction, respectively, where the probability of excitation is proportional to $|\mu\mathbf{E}|^2$. Higher excitation probability is depicted by lighter shades. The z-component of **E** (uniquely present in TIR evanescent illumination) selectively excites the regions of oblique membrane orientation. Note that the y-pol light equally excites all diI molecules only in this particular cross section, in which the local membrane normal is always parallel to the plane of the paper). However, other cross sections will be less excited by the y-pol light and more excited by x-pol light.

tation. However, in any single image, orientation information will be entangled with the effects of fluorophore concentration, fluorophore distance from the coverslip (which affects the local TIR illumination intensity), and geometrical foreshortening (more membrane area as projected on the substrate plane for oblique membrane). A ratio of images taken with two different excitation polarizations should divide out the effects of concentration, illumination intensity, and foreshortening, thereby leaving only effects of membrane orientation.

In TIR, the two readily available polarizations are *p*-pol (consisting mainly of *z*-pol with a slight amount of *x*-pol, as shown in Fig. 1) and *s*-pol (consisting of pure *y*-pol). In standard EPI illumination, the only two available polarizations are *x*-pol and *y*-pol. Ratio images of *p*-pol versus *s*-pol TIR excitation qualitatively highlight regions of membrane curvature with larger quotient values corresponding to oblique membrane and smaller values corresponding to substrate-parallel membrane. According to theoretical calculations, this *p*-pol/*s*-pol TIR ratio should display about three times the sensitivity to small angles of obliqueness than do *x*-pol/*y*-pol EPI ratios. At large angles of obliqueness, the *x*-pol/*y*-pol EPI ratio images theoretically should display more sensitivity to membrane orientation than the corresponding TIR ratio images. However, in typical biological samples, we wish to highlight regions that contain a submicroscopic mix of all membrane orientations, such as vesicles, blebs, or invaginations, as compared to substrate-parallel membrane. These mixed orientation regions will be excited to an equal extent by *x*-, *y*- or *z*-pol light. Because surrounding substrate-parallel membrane will be excited only weakly by *z*-pol light and excited strongly by *x*- and *y*-pol light, a ratio image of *p*-pol/*s*-pol excitation (the polarizations available in TIR illumination) will highlight vesicles, blebs, and invaginations as bright specks against a dark background (while normalizing against nonorientational effects). In contrast, a ratio image of *x*-pol/*y*-pol excitation (the polarizations available in EPI illumination) cannot distinguish between submicroscopic vesicles, blebs, and invaginations as compared to substrate-parallel membrane.

Two other features of TIR, unrelated to polarization, allow TIR to probe membrane orientation more sensitively than EPI. EPI illuminates both the upper and lower cell surfaces (i.e., distal and proximal to the substrate), with one of them possibly out of focus, whereas TIR illuminates only the lower membrane. This results in sharp focus and high contrast, even in the presence of fluorophores deeper within the cell. Also, because TIR images contain essentially no out-of-focus light, it is possible to deconvolute the images based on a 2D point spread function (PSF) that can be experimentally measured in the single TIR plane rather than the 3-dimensional (3D) PSF (and series of data images collected at several planes) necessary for EPI deconvolution. This simple deconvolution in the TIR plane, which can be performed on all images before any other processing, increases lateral resolution and contrast.

Quantitative theory

Dividing the image excited by *p*-pol evanescent light by the image excited by *s*-pol evanescent light produces a concentration- and illumination-independent ratio image that depends solely on membrane orientation. To translate the observed ratios to quantitative information regarding membrane orientation, several steps must be considered: 1) the dependence of diI orientation on membrane orientation and rotational diffusion; 2) the ellipticity of the excitation polarization; 3) the anisotropic pattern of dipole emission and microscope collection; and 4) integration over all relevant diI orientations at the times of absorption and emission.

The theory below does not consider the effects of a spatially variable index of refraction in the cytoplasm. These effects can include both spatial variations in the depth and intensity of the evanescent field and also light scattering. Light scattering can lead to the conversion of a fraction of the evanescent light into propagating light; however, this fraction appears to be very small (Axelrod et al., 1992).

DiI orientation: dependence on membrane orientation and rotational diffusion

The orientation of the absorption or emission transition dipoles of membrane-intercolated diI relative to the optical system is a function of the orientation of the membrane with respect to the optical system, the orientation of diI with respect to the membrane, and the orientations of the transition dipoles with respect to a diI-fixed frame. We define two sets of coordinate axes, the "lab" frame (with orientation fixed to the optical system), and the "membrane" frame (with variable orientation according to the local membrane inclination) (see Fig. 3, *a* and *b,* respectively). In the lab frame (unprimed axes), the *z* axis is normal to the substrate, the *x* axis is in the plane of incidence formed by the incident and reflected TIR beams (with its positive direction in the

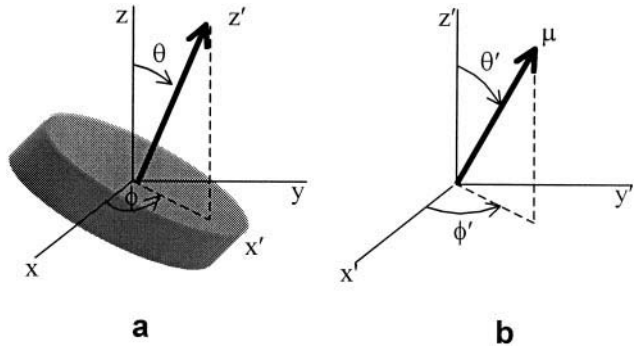

FIGURE 3 The coordinate system used to describe fluorophore orientation. (*a*) The membrane orientation (*disk*) and membrane-fixed axis system (*prime axis*) relative to the coordinate system defined by the normal to the TIR substrate (*z*) and the plane of TIR incidence (*x–z*). (*b*) The orientation of a transition dipole (μ) relative to the local normal to the membrane plane. Note that the membrane orientation is completely specified by the angles θ and ϕ and that the dipole direction relative to the membrane is completely specified by the angles θ' and ϕ'.

direction of evanescent wavefront motion), and the y axis is perpendicular to the plane of incidence. In the membrane frame (primed axes), the z' axis is the normal to the local membrane tangent plane, and the x' axis is in the z–z' plane. Viewed from the lab frame, the membrane frame's z' axis is oriented at polar angle θ (measured from the z-axis) and azimuthal angle ϕ (measured from the x axis). The goal of the p-TIRF technique is to measure the membrane orientation relative to the substrate plane in terms of θ and ϕ.

An assumption in this paper is that the diI is intercolated into the membrane with its linear conjugated bridge parallel to the membrane surface, so that rotation of the diI molecule has no effect on the polar angles of absorption or emission with respect to the local membrane normal. The diI transition dipoles are assumed to be distributed with azimuthal symmetry around the local z' axis normal to the plane of the membrane; the azimuthal angle as measured from the x'-axis is denoted as ϕ'. For each diI molecule at a fixed time, the absorption and emission dipoles are assumed to lie in the same plane that also includes the membrane normal. The transition dipole's polar angle with respect to the normal to the membrane (the z' axis) is referred to as θ'. For dipoles lying exactly in the plane of the membrane, $\theta' = 90°$. The fluorophore-containing group of diI (the head group) is mirror-symmetric around the long axis parallel to the hydrocarbon tails. This means that, if an absorption or emission transition dipole is oriented at θ', there will be an equal amplitude dipole oriented at $180 - \theta'$ (Axelrod, 1979).

The polar angles of the absorption and emission dipoles, $\theta'_{a,e}$, respectively, are not necessarily colinear in a fixed diI molecule, and therefore the angles θ'_a and θ'_e are somewhat free parameters for fitting the theory to experimental results, within the constraints of previous time resolved anisotropy measurements (see Appendix A). The diI molecule may rotationally diffuse in ϕ' around the membrane normal between the events of absorption (at $\phi'_a = \phi'_0$) and emission (at $\phi'_e = \phi'_1$).

Given the orientation of the transition dipole (either absorption or emission) with respect to the membrane characterized by angles θ' and ϕ', and orientation of the membrane with respect to the lab characterized by angles θ and ϕ, a unit amplitude transition dipole vector μ can be expressed in Cartesian coordinates as (see Appendix B)

$$\boldsymbol{\mu} = \begin{pmatrix} \mu_x \\ \mu_y \\ \mu_z \end{pmatrix} \tag{1}$$

where $\mu_x = \cos\theta\cos\phi\sin\theta'\cos\phi' - \sin\phi\sin\theta'\sin\phi' + \sin\theta\cos\phi\cos\theta'$, $\mu_y = \cos\theta\sin\phi\sin\theta'\cos\phi' + \cos\phi\sin\theta'\sin\phi' + \sin\theta\sin\phi\cos\theta'$, and $\mu_2 = -\sin\theta\sin\theta'\cos\phi' + \cos\theta\cos\theta'$. The dipole can undergo rotational diffusion through azimuthal angles ϕ' around the normal to the membrane in the time interval (~0.2 ns) between excitation (ϕ'_0) and emission (ϕ'_1). If the molecule is excited at angle ϕ'_0 at $t = 0$, the probability density P_1 that the dipole emits from angle ϕ'_1 at time t is a product of the exponentially decaying probability density that the fluorophore emits exactly at time t and the probability density (see Velez and Axelrod, 1988) that the fluorophore has rotationally diffused from ϕ'_0 to ϕ'_1 in time t,

$$P_1(\phi'_1 - \phi'_0, t) = (\pi\tau)^{-1} e^{-t/r}\left[\sum_{n=0}^{\infty}\left(\frac{\delta_{n0}}{2} + \cos n(\phi'_1 - \phi_0)\right) e^{-n^2 D t}\right], \tag{2}$$

where ϕ_{n0} is unity for $n = 0$ and zero otherwise; D is the rotational diffusion coefficient; and τ is the fluorescence lifetime. Based on steady-state diI-polarization measurements in erythrocyte membranes, Axelrod (1979) inferred the average change of angle during the excited state lifetime ($= D\tau$) to be ~0.27 radians.

Evanescent field polarization

Incident light polarized normal to the plane of incidence (s-pol) produces an evanescent field $\mathbf{E}_s = E_y\mathbf{y}$, where E_y is a function of the incidence angle and indices of refraction (Hellen et al., 1988). Incident light polarized in the plane of incidence (p-pol) produces an elliptically polarized evanescent field $\mathbf{E}_p = E_x\mathbf{x} + E_z\mathbf{z}$, where E_x and E_z depend upon incidence angle (Hellen et al., 1988). In general, E_z is considerably larger than E_x. As the incidence angle approaches the critical angle, E_x approaches zero and the p-pol evanescent field thereby approaches pure z-polarization. In our cell experiments, the incidence wavelength (in vacuum) is 514.5 nm and the incidence angle is 70.5° at a glass-cell (refractive index ratio 1.517/1.38) interface, thereby giving the evanescent electric field (for an incident electric field of unit amplitude)

$$\mathbf{E}_s = (1.61\,\mathbf{y})\cdot e^{-z/2d}, \tag{3a}$$

$$\mathbf{E}_p = (0.44\mathbf{x} + 1.70i\mathbf{z})\cdot e^{-z/2d}. \tag{3b}$$

The $\mathbf{E}_s$ and $\mathbf{E}_p$ fields are shown schematically in Fig. 1. The imaginary i factor in the z component reflects that the x and z components are $\pi/2$ out of phase (Hellen et al., 1988; Axelrod et al., 1992). This phase factor for p-pol light ensures that the excitation probability $|\mu\cdot\mathbf{E}_p|^2$ is $(\mu_x E_x)^2 + (\mu_z E_z)^2$ with no cross terms. For s-pol light, $|\mu\cdot\mathbf{E}_s|^2$ is $(\mu_y E_y)^2$. The excitation intensities $I_{p,s}$ are $|\mathbf{E}_{p,s}|^2$, and both polarizations decay exponentially in z with the same characteristic distance d, where d depends on the relative indices of refraction, the wavelength, and the incidence angle. For $\theta = 70°$ at a glass/cell interface, the characteristic depth d is 114 nm.

Anisotropic emission and collection pattern

We define P_2 to be the fraction of emitted fluorescence power from an excited diI fluorophore that is collected by an objective lens, relative to the total fluorescence power emitted by that fluorophore. P_2 is a complicated function of the index of refraction n in which the fluorophore resides,

the distance z_0 from the coverslip, the emission dipole orientation at $\{\theta, \phi, \theta'_e, \phi'_1\}$, and the objective's numerical aperture A.

There are several considerations in determining P_2. 1) Only light propagating up to a maximum angle determined by A and n is collected. 2) The emission pattern of a dipole near an interface (i.e., less than one wavelength away) is different from the $\sin^2$ emission pattern of an isolated dipole (Ford and Weber, 1984; Hellen and Axelrod, 1987). We calculate that this effect alters P_2 by at most 20% for glass-water interfaces. Proximity to an interface causes P_2 to depend on the distance from the interface in addition to the fluorophore's emission dipole angle with respect to the interface normal. 3) The emitted light in our optical configuration transmits through several glass-water interfaces before it reaches the objective. The transmission coefficient depends upon polarization, but this dependence alters P_2 by only ~2%. Appendix C describes the calculation of P_2 in further detail.

Integration over relevant dil orientations

The observed fluorescence intensity from a single diI dipole incorporated into a membrane is proportional to the product of its excitation probability and the fraction of its emitted power that is captured by the objective. The excitation probability of the dipole is proportional to $|\boldsymbol{\mu} \cdot \mathbf{E}|^2$, where $\boldsymbol{\mu}$ is given by Eq. 1 and $\mathbf{E}$ is given by Eq. 3. The probability we observe the emission of an excited dipole oriented with angles $\{\theta, \phi, \theta'_e, \phi'_1\}$, is the numerical aperture-dependent function P_2 (cos β, z_0) where cos $\beta = \boldsymbol{\mu}(\theta, \phi, \theta'_e, \phi'_1) \cdot \hat{z}$.

The observed fluorescence intensity $F_{s,p}(\theta, \phi, z_0)$ from a diI-labeled membrane oriented at $\{\theta, \phi\}$ is an integral of the intensity resulting from a single diI molecule oriented at $\{\theta'_e, \phi'_0\}$ with respect to the membrane, integrated over ϕ'_0, the isotropic distribution of diI molecules around the local membrane normal. Since the dipole may rotate during excitation, we also must integrate over all possible emission azimuthal angles ϕ'_1, weighted according to the rotational diffusion probability density given by Eq. 2. Then, the observed fluorescence F (with all factors of quantum efficiencies, unit conversions, and numerical constants suppressed) is

$$F_{s,p}(\theta, \phi, z_0) = \int_{\phi'_0, \phi'_1, t} |\boldsymbol{\mu}(\theta, \theta'_a, \phi, \phi'_0) \cdot \mathbf{E}_{s,p}(z_0)|^2 P_1(\phi'_1 - \phi'_0, t) \times P_2(\cos\beta, z_0) \; d\phi'_0 \, d\phi'_1 \, dt. \quad (4)$$

The right side of Eq. 4 was numerically integrated in Fortran. Fig. 4 *a* shows the numerically computed $F_{s,p}$ as a function of membrane orientation $\{\theta, \phi\}$ assuming the following particular parameters: TIR incidence angle = 70°; θ'_a = 76.5° and 103.5°, and θ'_e = 80° and 100° (see Appendix A); $D\tau$ (used in P_1) = 0.27; and P_2 calculated assuming a 1.0 numerical aperture (A) objective. Note that F_p is strongly dependent on θ, with a minimum at $\theta = 0$ (substrate-parallel membrane). As seen in Fig. 4 *a*, F_p and F_s vary significantly with both θ and ϕ, generally with opposite tendencies. For example, consider the $\phi = 90°$ curves shown in Fig. 4 *a*: as θ varies from 0 to 90°, F_s decreases by a factor of 17 and F_p increases by a factor of 3. Fig. 4 *b* shows the ratio F_p/F_s versus $\{\theta, \phi\}$. Note also that ϕ has an increasingly larger effect as θ increases.

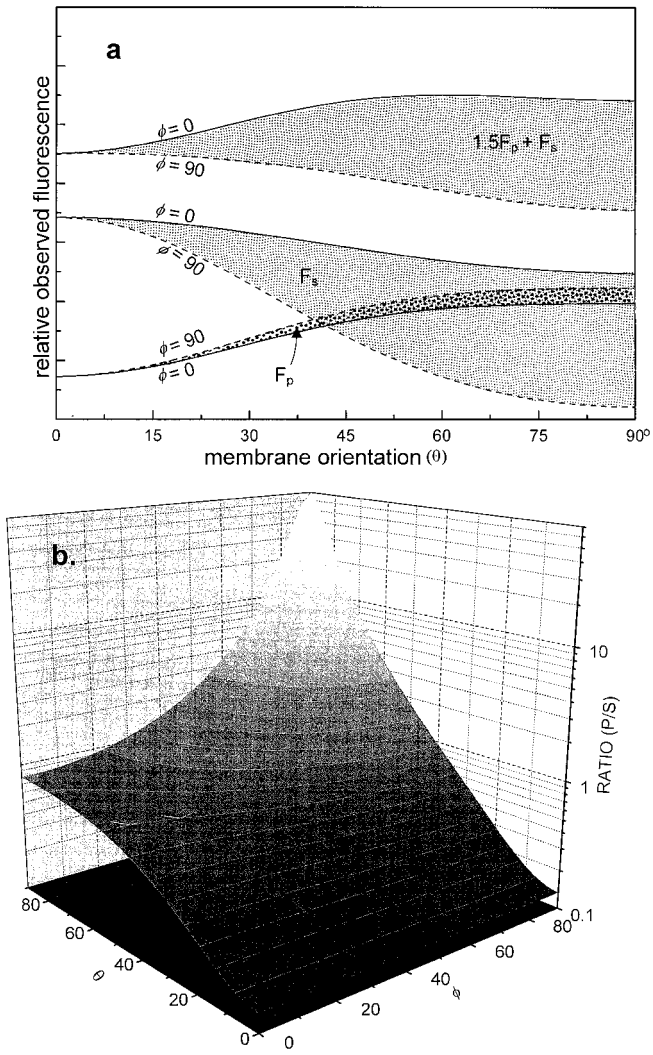

FIGURE 4 (*a*) The numerically computed observed fluorescence intensity (arbitrary units) as a function of membrane orientation $\{\theta, \phi\}$ (in degrees) assuming the particular parameter values discussed in the text. The darkest shaded region displays F_s, where the top line marks $\phi = 0°$ and the bottom line marks $\phi = 90°$; the medium gray shaded region displays F_p, where the bottom line marks $\phi = 0°$ and the top line marks $\phi = 90°$. The lightest gray shaded region displays the calculated quantity 1.5 F_p + F_s, a quantity chosen because it has the least variation between substrate-parallel and vesicle membrane configurations. (*b*) The *p*/*s* ratio (F_p/F_s) versus $\{\theta, \phi\}$ shown in a 3D graph format for the same parameter values.

In general, the observed TIRF intensity depends on the dipole orientational distribution (which can vary over x, y, and z, as is typical in labeled membranes) and not just on the

local fluorophore concentration and distance from the coverslip. Although not specifically used in the analyses of this paper, some linear combinations of F_p and F_s can be found that vary much less than F_p and F_s individually over the range of all membrane orientations. One such linear combination, $(1.5\ F_p + F_s)$ (also plotted in Fig. 4 *a*), differs by less than 1% between a substrate-parallel membrane and the same area of membrane configured into a submicroscopic spherical vesicle (the two configurations expected to be encountered most often in our experiments). This linear combination minimizes sensitivity to membrane orientation while preserving sensitivity to concentration and distance from the coverslip. In contrast, the ratio F_p/F_s preserves sensitivity to membrane orientation while eliminating dependence on concentration and distance from the coverslip. The combination $1.5\ F_p + F_s$ could most easily and accurately be obtained by the appropriate polarization of a single illuminating beam.

In actual samples, light collected from a particular pixel is not expected to result from a membrane purely oriented at one orientation only $\{\theta, \phi\}$, but that it rather results from some mixture of membrane orientations. We define the measured fluorescence intensity $\mathcal{F}_{s,p}$

$$\mathcal{F}_{s,p} = \int_{\theta}\int_{\phi} F_{s,p}(\theta, \phi, z_0)\rho(\theta, \phi, z_0)\, d\theta\, d\phi, \qquad (5)$$

where ρ is the amount of membrane oriented $\{\theta, \phi\}$ in the volume of sample measured at a particular pixel. In this paper, ρ is assumed to be a linear combination of the delta function $\delta(\theta = 0)$ (corresponding to substrate-parallel membrane) and a constant (corresponding to membrane oriented in a submicroscopic spherical vesicle). Theoretical fluorescence intensities $\mathcal{F}_s$, $\mathcal{F}_p$, and $\mathcal{F}_p/\mathcal{F}_s$ for some typical hypothetical samples are shown in Table 1, including both diI in membranes and fluorophores (with colinear absorption and emission dipoles) oriented isotropically in 3D solutions or adsorbed to glass. Given the measured fluorescence values $\mathcal{F}_{s,meas}$, $\mathcal{F}_{p,meas}$ in a particular pixel, the relative amounts of membrane in substrate-parallel and spherical configurations (*a* and *b*, respectively) can be calculated with the equations,

$$\begin{aligned} \mathcal{F}_{s,meas} &= a\,\mathcal{F}_{s,par} + b\,\mathcal{F}_{s,sphere}, \\ \mathcal{F}_{p,meas} &= a\,\mathcal{F}_{p,par} + b\,\mathcal{F}_{p,sphere}, \end{aligned} \qquad (6)$$

where $\mathcal{F}_{s,p}$ for the substrate-parallel and spherical cases are given in Table 1.

METHODS

Several different sample preparations were used: 1) aqueous solutions of rhodamine-dextran (r-dextran) and fluorescein; 2) diI adsorbed to glass; 3) rhodamine bovine serum albumin (R-BSA) adsorbed to glass; 4) glass-supported phospholipid bilayers containing diI; 5) erythrocytes with diI-labeled plasma membranes; 6) macrophages loaded with r-dextran; and 7) macrophages with diI-labeled plasma membranes. For all these sample types, the same TIR microscope optical configuration was used.

TABLE 1 Theoretical calculation for observed fluorescence $\mathcal{F}_{p,s}$, when excited by a *p*-pol or *s*-pol TIR beam using Eq. 5 and parameters as described in the text

Membrane (ρ), or Dipole Orientational Distribution	z_0 (nm)	n	$\mathcal{F}_p$	$\mathcal{F}_s$	Ratio $\mathcal{F}_p/\mathcal{F}_s$
diI Embedded in planar membrane	4	1.33	0.053	0.192	0.28
		1.38	0.052	0.254	0.21
diI Embedded in a spherical vesicle membrane, averaged over the sphere, $D\tau = 0.27$	4	1.33	0.093	0.101	0.92
		1.38	0.113	0.133	0.85
diI Embedded in a spherical vesicle membrane, averaged over the sphere, $D\tau \sim \infty$	4	1.33	0.099	0.098	1.01
		1.38	0.122	0.128	0.96
Isotropic in 3D, nonrotating	Average over all z_0	1.33	0.103	0.102	1.01
		1.38	0.119	0.131	0.91
Isotropic in 3D, nonrotating	4	1.33	0.093	0.107	0.87
		1.38	0.111	0.141	0.79
Isotropic in 3D, fast rotating	Average over all z_0	1.33	0.128	0.091	1.41
		1.38	0.155	0.116	1.34

The fluorescence units are arbitrary and reflect the relative observed fluorescence per unit fluorophore; a substrate-parallel unit fluorophore excited by an *s*-pol TIR incidence beam in $n = 1.38$ medium results in a $\mathcal{F}_s$ of 0.254. Parameter z_0 is the dipole's distance from the substrate, and calculations are done for two different sample indices of refraction n. In general, the collection efficiency from an excited fluorophore depends on its orientation with respect to the surface normal, its rotation parameter $D\tau$, and its distance from the coverslip z_0. However, the ratio of the observed fluorescence collected from a particular fluorophore excited by *p* versus *s*-polarized light does not depend on any of these parameters; that ratio depends only on the relative probabilities of excitation in the two polarizations. For a flat substrate-parallel membrane with incorporated diI (in which all the dipoles are assumed to reside at the same angle with respect to the substrate normal), all the fluorophores have the same ratio of probabilities for *p*- versus *s*-polarized excitation, with the *p*/*s* ratio being z_0-independent. Rotation confers an advantage on observing the fluorescence from *p*-pol excitation, because light emitted from dipoles that are oriented to best absorb *p*-pol light is least likely to be observed by our objective (see Fig. C1).

Optical configuration

Fig. 5, *a* and *b* show the optical configuration for TIR fluorescence used here. Based around an inverted microscope, the TIR system uses an inexpensive commercial 45–45–90° triangular prism that allows entry of the light into the coverslip cell substrate at incidence angles higher than achievable by prismless (through the lens) TIR excitation in $n = 1.52$ glass objectives (Stout and Axelrod, 1989). Once trapped inside the coverslip (which actually consists of two #2 coverslips in optical contact by a layer of immersion oil), the beam totally internally reflects several times. We used the third or fourth reflection at the upper surface. Lateral translation of the sample is facilitated by sliding the bottom coverslip on the top face of the prism. (Another possibility is to slide the upper coverslip of the pair upon the lower one, which could be kept fixed relative to the prism.). The relatively thick, double coverslip combination allows successive reflections to be well separated, but not so thick as to preclude the use of moderately short working distance objectives.

This configuration is particularly convenient for cell cultures, because the sample chamber containing the cells (adhered to a coverslip) is completely accessible from above for solution changes and microinjection. This configuration also permits the use of incidence angles great enough to ensure that TIR occurs even at local regions of high refractive index in the submembrane cytoplasm. However, only water- or air- but not oil-immersion objectives may be used.

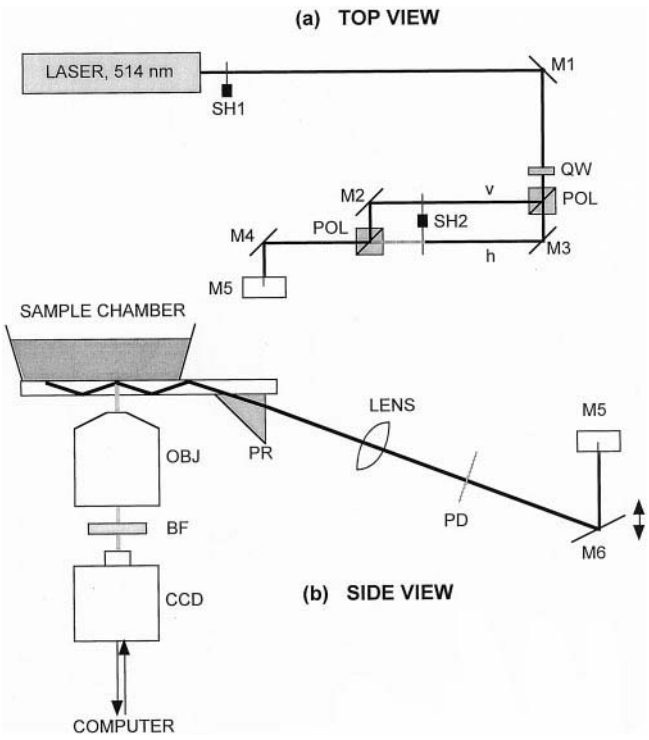

FIGURE 5 Optical configuration for polarized TIRF. (*a*) Top view of the beam path from the Ar laser (Spectra Physics 2020) to mirror M5, at which the beam is reflected vertically down. (*b*) Side view from mirror M5 to the region below the sample chamber. Except for the objective, the standard inverted microscope (Leitz Diavert) upon which the sample chamber rests is not shown explicitly; the CCD camera (Photometrics Star-1, 576 × 384 pixels) is actually mounted atop the microscope's trinocular viewing head. Abbreviations are: SH1, electric shutter; M1–M6, planar mirrors; QW, quarter wave plate to convert the laser beam polarization from vertical to circular; POL, polarizing cubes to separate and then recombine beam paths for horizontal (h) and vertical (v) polarization; SH2, electric shutter for blocking either the horizontal or vertical beam paths; PD, glass plate for deflection of a small fraction of the intensity to a photodiode; PR, 5 × 5 × 5 mm right angle standard optical glass prism (Edmund Scientific); BF, colored glass barrier filter.

Preparation of coverslips

For all the preparation types, 25-mm-diameter #2 standard coverslips were soaked in H_2SO_4 overnight in a porcelain holder, and then rinsed under a distilled water (dH_2O) drip for at least 2 h followed by drying in an oven (130°F). Coverslips were used within 24 h of treatment. Opsonized coverslips were prepared by the method of Swanson et al. (1992).

Fluorescent bulk solutions

R-dextran with average molecular weights of 10,000 or 70,000 (Molecular Probes, Eugene, OR), and fluorescein (Research Organics, Cleveland, OH) were each dissolved in Dulbecco's phosphate buffered saline with 1 g/L glucose (PBSg) buffer (Grand Island Biological Co., Grand Island, NY) to a final concentration of 10 μg/mL.

The sample chamber was assembled from three coverslips, two on the bottom in optical contact with oil, and one on the top separated by a 60-μm Teflon spacer. The sample chamber was squeeze-mounted with spring clamps on an aluminum plate over a drilled hole. When viewed on the stage of the TIR microscope, fluorescence could be seen both from fluorophores dissolved in the bulk within the evanescent field depth and also from fluorophores adsorbed to the surface. The former produced a diffuse glow showing only the features of the illumination profile; this pattern remained unchanged as the sample was moved laterally. The latter produced fluorescence with fine details corresponding to irregularities and fine scratches in the glass. The adsorbed fluorophores appeared largely irreversibly bound; adsorbed fluorescence could be photobleached away with prolonged bright TIR illumination before data was taken. In contrast, dissolved fluorescence recovered extremely rapidly by diffusion after such a bleach.

DiI adsorbed to glass

A few drops of a solution of 0.5 mg/mL diI in ethanol were placed on a coverslip and then immediately washed off with dH_2O. This coverslip, with its diI coating face up, formed the top component of the two-coverslip-thick TIR substrate.

R-BSA adsorbed to glass

Bovine serum albumin (BSA) (Miles Laboratories, Naperville, IL), dissolved at 1 mg/mL in PBSg was incubated with 5′ and 6′ carboxymethylrhodamine (Molecular Probes) at a 3:1 dye:protein molar ratio for 1 day, and then run down a Sephadex G-25 column made in PBSg to separate the protein from the unbound rhodamine. Acid-treated coverslips were exposed to this r-BSA for 30 min and then washed with dH_2O.

Supported lipid bilayers with incorporated diI

Coverslips were prepared as in Mc Kiernan et al. (1997), followed by a 5-min plasma cleaning (Harrick Scientific, Ossining, NY) with ionized argon gas. Phosphatidylserine/phosphatidylcholine (PS/PC, at a 1:3 molar ratio) supported bilayers on glass were deposited on these coverslips by introducing a sonicated suspension of lipid into a sandwich of two coverslips separated by a 60-μm Teflon spacer.

Bilayer membranes were labeled by diI as follows. The bilayer membrane/coverslip sandwich was incubated in a humid environment for 1 h and then rinsed four times with PBS by capillary flow-through. Then, 35 μL of a diI ethanolic dispersion (0.5 mg/mL diI in 95% ethyl alcohol was diluted 100-fold in deionized water) was introduced into the coverslip sandwich. After 45 min, the sandwich was rinsed four times with 70 μL PBS buffer. By this procedure, diI becomes irreversibly incorporated into the membranes on the inner surfaces of the coverslip sandwich. The membranes, however, remain intact and contiguous, as can be confirmed by an observed 100% fluorescence recovery after photobleaching using a standard focused spot.

Erythrocytes adhered to glass

One drop of human blood (obtained by fingertip lance) was suspended in 1 mL PBSg, to which 20 μL of 0.5 mg/mL diI in ethanol was subsequently added and stirred. The mixture was incubated at 37°C for 30 min and centrifuged at low speed. The labeled erythrocyte pellet was then washed and centrifuged twice with PBSg to remove free diI. The cells were suspended in PBSg buffer and allowed to settle on acid-treated coverslips and then mounted as in the above samples. (Cells plated on untreated coverslips were observed to flicker rapidly in and out of the evanescent field.) In some samples, 1 mg/mL BSA was added to the PBSg; this tends to convert misshapen or crenated erythrocytes to biconcavity.

Macrophages adhered to glass

Bone marrow-derived macrophages from C3H-HeJ mice (Jackson Laboratories, Bar Harbor, ME) were obtained as described previously (Swanson, 1989). Macrophages from six-day-old cultures were resuspended in cold PD buffer (137 mM NaCl, 3 mM KCl, 1 mM KH_2PO_4, 6 mM Na_2HPO_4, pH 7.4), then plated either into 35-mm diameter dishes for later resuspension or onto coverslips. Plated cells were maintained overnight in Dulbecco's modified Eagle's medium containing 10% heat-inactivated fetal bovine serum (DMEM/10F) (Grand Island Biological Co.). Macrophages on coverslips were maintained in RB buffer (155 mM NaCl, 5 mM KCl, 2 mM $CaCl_2$, 1 mM $MgCl_2$, 2 mM NaH_2PO_4, 10 mM HEPES, pH 7.2, 10 mM glucose).

Coverslip mounting was somewhat different for the macrophages than for the above samples. Plastic culture dishes, 35 mm, were drilled out with a ¾″ hole and an acid treated coverslip was glued onto the outside of the dishes with Sylgard 182 epoxy resin (Dow Corning Corp., Midland, MI). After this, the coverslip was opsonized if needed and incubated in medium before macrophage plating. A layer of mineral oil was placed on top of the medium to minimize evaporation and loss of CO_2.

For labeling macrophages with diI, macrophages adhered in plastic tissue-culture dishes were first rinsed once with RB buffer. Then 1 mL RB buffer was added and 20 μL of 0.2 mg/mL diI in ethanol was added and stirred. After an incubation for 5 min at 37°C, the cells were rinsed once with PD buffer (which promotes release of adherence), then 1 mL PD buffer was added, and the suspension was chilled for 10 min on ice. To suspend the cells, the suspension was then triturated vigorously at least 25 times with a 1-mL plastic pipette. After dilution to a concentration of no more than 0.1 mL labeled cell suspension per 1 mL DMEM/10F, the diluted suspension was then added to the drilled coverslip dishes to incubate for one h at 37°C.

Macrophages were scrape-loaded with r-dextran according to published methods (Hollenbeck and Swanson, 1990; McNeil et al., 1984). The medium was removed from adhered macrophages, saved for later use, and the cells were rinsed twice with PD buffer. All of the PD buffer was removed and immediately replaced with 20 μL buffer (PD or RB) containing 10 mg/mL r-dextran (molecular weight 10,000; Molecular Probes). After this solution was gently spread over the cells, a rubber policeman was used to scrape all the adhered cells from the dish, with scraping motion performed in one direction only. Then, the medium was poured back into the dish and swirled. The resulting scrape-loaded cell suspension was then dispensed into the drilled coverslip dishes to incubate for one h at 37°C to allow cell spreading.

Data collection

All data were collected at room temperature using a custom MS-DOS-based Fortran/assembly language program that controls the charge coupled device (CCD) camera shutter, image recording, interframe time, beam block shutter (SH1), and polarization toggle shutter (SH2). The program's commands are sent to programmable output pins on a counter/timer board (Computer Boards Inc., Middleboro, MA) to which the hardware devices are connected. Because

of the high degree of fluorophore orientation in diI-labeled membranes, the measured fluorescence of the *p*-pol images (i.e., the image excited by *p*-pol light) is much less than that of the *s*-pol images. For this reason, *p*-pol images were often exposed four times longer than *s*-pol images to make sure both images had similar signal/noise ratios. The Photometrics Star-1 camera system used here could record up to one frame every 6 s. Exposure times ranged from 0.4 to 1.6 s under low illumination. The pixel size was 0.25×0.25 μm with our 50× objective.

Ratios of images

A background correction for each image was achieved by selecting an off-cell region in the beam and subtracting its average count per pixel from each pixel in the whole region of interest. The modified *p*-pol image was divided by the modified *s*-pol image to produce a ratio image (the *p*/*s* ratio) containing information about the membrane orientation but with the effects of concentration and *z*-dependent variations divided out.

Accuracy of measurements

Sources of error in the ratio images are: sample motion between frames, shot noise and CCD readout noise, misalignment of the excitation beams, and bleaching. Shot noise and CCD noise for a given pixel should account for about 1% error in our images, but this can be reduced by signal averaging. Frame-to-frame bleaching was observed to be less than 0.5%. Sample motion between frames is observed in some images; for quantitative analysis, ratios were used only if they remained constant over several frames. Relative misalignment of the two polarizations is observed to create up to 15% variation in the observed ratio of a uniform sample over distances comparable to cellular size, making this the largest source of error. A 15% error in the observed ratio corresponds to an uncertainty of 10° in the membrane orientation for membrane that is nearly substrate parallel. Differences between nearby pixels are expected to have less than 1% error, resulting in less than 2° of uncertainty in the membrane orientation difference.

Image sharpening by deconvolution

Areas surrounding fluorescently labeled cells showed a decaying haze of fluorescence beyond the borders of the cell, suggesting that the experimental point spread function (PSF) of our setup has a long tail. This type of effect could blur interesting features in the images and make the observed range of ratios smaller than the actual range. Therefore, we experimentally measured an actual 2D PSF as formed by the images of TIR-excited diI-labeled submicroscopic 0.1-μm-diameter glass beads (Seragen Diagnostics, Indianapolis, IN), and used the fit of these experimental PSFs to deconvolute our images with standard Fourier deconvolution (Shaw and Tigg, 1994). A 2D PSF is indicated in TIR because the observed fluorescence is emitted from a single focal plane.

The glass beads were labeled with diI as follows. Glass beads 20 μL were incubated with 20 μL 0.5 mg/mL diI in ethanol for 30 min. Then, 1 mL of dH_2O was added and sonicated until translucent. This solution was further diluted and deposited onto acid-treated coverslips. Because the beads do not adhere strongly to the coverslip glass, the liquid was withdrawn after 5 min and TIR fluorescence CCD images of individual beads at the glass-air interface were recorded.

The images of diI-coated beads were found to fit well to a Lorentzian function. Trial Lorentzian PSFs of varying widths were tested by deconvoluting an image of a submicroscopic bead, with the requirement the deconvoluted image should contain a minimal point spread, minimal halos, and few negative values. Each deconvoluted image was quantitatively evaluated by a parameter Q, which decreases with improved quality of the deconvoluted image,

$$Q = \frac{\sum_{x,y} |I(x,y)| \sqrt{x^2 + y^2}}{\sum_{x,y} I(x,y)}. \tag{7}$$

The origin ($x, y = 0$) is defined by the brightest pixel, and $I = 0$ is defined by the intensity far from the bright locations. It is important to take the absolute value of the intensity, because a negative influence at one location should not cancel a positive influence at another location; in practice, the intensity was summed over all I values at a particular $(x^2 + y^2)^{1/2}$ before the absolute value was taken to reduce the effects of noise.

An additional criterion is that the deconvolution should produce no negative halos or other obvious defects: such halos can produce large erratic quotients during ratio-taking. We have found that these artifacts can result from pixelization. An $n \times n$ pixel image of a Lorentzian deconvoluted with itself should and does result in a delta function. The center of the Lorentzian may be at the center of a pixel, between two pixels, or at any other subpixel location. However, unless the image used for deconvolution is centered at the same subpixel location as the image to be deconvoluted, the resulting deconvoluted image contains artifacts, including negative halos. An actual image will contain fluorophores at many subpixel locations, and thus, artifacts are expected to result from deconvolution unless a less aggressive deconvolution PSF is used.

The final PSF used for deconvolution was a combination of a Lorentzian of width 0.6 pixels (0.18 μm) and a delta function at the center of the PSF of height equal to 5% of the total PSF intensity. This resulted in an ~40% improvement in Q over the original bead images, with few negative values. The resulting images on both beads and cells are noticeably sharper, with few defects, than the original images. Figure 6 shows the intensities of a one-dimensional scan across the edge of a diI-labeled macrophage cell for the original (*open circles*) and deconvoluted (*closed circles*)

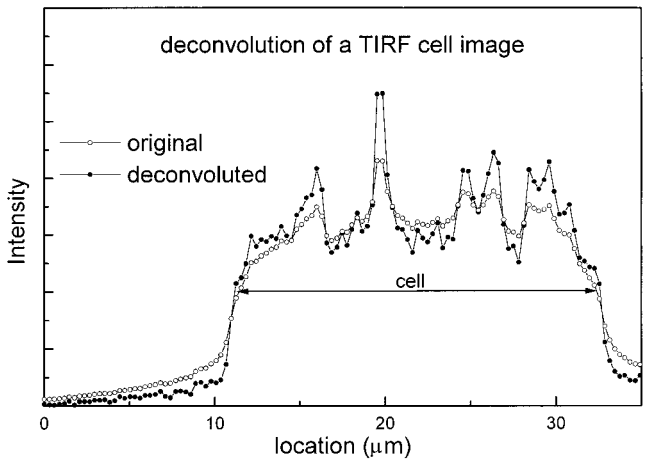

FIGURE 6 Effect of deconvolution at the edge and interior of a diI-labeled macrophage. This is a scan transverse to the edge of a macrophage showing the intensity of the *p*-pol image for the original (*open circles*) and deconvoluted (*closed circles*) images. Note the deconvoluted edge is sharper with less halo.

images. Note that the deconvoluted image has a much less pronounced positive intensity halo outside the cell edge.

RESULTS

The polarized TIR technique was tested on two main sample types: (I) spatially uniform and nearly orientationally isotropic in vitro solutions and adsorbates, and (II) spatially variegated and/or orientationally anisotropic systems, including microinjected cells, and diI in model and biological membranes and living cells with numerous and dynamic morphological features. For the generally featureless samples in group I, only quantitative results are presented; for the variegated samples in group II, both quantitative results and, in some cases, images are presented.

Group I: spatially uniform and nearly isotropic in vitro samples

Table 2 shows experimentally observed *p*/*s* ratios for some nonmembrane in vitro systems, along with a comparison to theoretically expected values. The theoretical values are expressed as a range (as explained in the footnote) because certain key parameters (such as diI dipole angle with respect to the membrane, or rotational diffusion rate of a fluorophore) are not precisely known.

In general, the lower the ratio, the more parallel the fluorophore dipoles are to the substrate. In most cases, the measured ratio falls within the theoretical range. The only measured ratio that is unexpectedly low is for BSA absorbed to glass in air. One interpretation of this result is that BSA and its attached fluorophore dipoles become more flattened on the surface when water is removed.

TABLE 2 Experimentally observed *p*/*s* ratios for nonmembrane in vitro systems

Sample Type	Fluorophore	*p*/*s* Ratio Observed	*p*/*s* Ratio Theoretical Range*
r-BSA on glass (air) ($n = 10$)	rhodamine	0.88 ± 0.04	1.2–1.6
r-BSA on glass (PBSg) ($n = 20$)	rhodamine	0.90 ± 0.09	1.01–1.41
diI on glass (air) ($n = 10$)	diI	0.71 ± 0.04	0.51–1.2
diI on glass (PBSg) ($n = 20$)	diI	0.62 ± 0.03	0.16–0.92
R-dextran, mw 10,000, in PBSg ($n = 11$)	rhodamine	0.96 ± 0.01	1.01–1.41
R-dextran, mw 70,000, in PBSg ($n = 10$)	rhodamine	0.97 ± 0.02	1.01–1.41
Fluorescein in PBSg ($n = 4$)	fluorescein	1.10 ± 0.02	1.01–1.41

*The theoretical ranges are given for the following conditions: for r-BSA on glass, r-dextran solutions, and fluorescein solution, the lower limit assumes colinear fixed absorption and emission dipoles, and the upper limit assumes rapid isotropic rotation during the excited state lifetime. For diI on glass, the lower limit assumes the diI absorption dipole angle is parallel to the plane of the coverslip and the upper limit assumes a fixed isotropic distribution in three dimensions. In the fluorescein solution sample only, some adsorption to the glass surface was noted (~5% of the total intensity); this surface fluorescence was bleached away before data were acquired.

Group II: spatially variegated or orientationally ordered systems

Table 3 shows experimentally observed *p*/*s* ratios for labeled model membranes and biological cells. In each case, *p*/*s* ratios for both deconvoluted and original images are presented. Expected theoretical values are given, again with ranges as explained in the footnote. In addition, the rightmost column shows how the measured deconvoluted ratios can be interpreted as arising from a weighted mix of membrane that is oriented parallel to the substrate and membrane in a spherical configuration.

DiI in supported phospholipid bilayers

A surprising result is that diI in supported phospholipid bilayers is not as ordered as diI in erythrocytes. Assuming that diI in erythrocytes is completely ordered (i.e., all of the diI is intercolated into the membrane with its linear conjugated bridge parallel to the membrane surface), then at least 24% of the diI in a PC/PS supported bilayer can be interpreted as being in a random orientational distribution.

Erythrocytes

Erythrocytes provide a good test of the p-TIRF method because their surfaces are relatively smooth and free of ruffles, endo- or exocytotic sites, and their overall shape is

TABLE 3 Experimentally observed *p/s* ratios for dil-labeled model membrane, dil-labeled erythrocyte membrane, and macrophage samples

Sample Type	Fluorophore	Location	Original Image	Deconvoluted Image	Substrate-parallel (%)
Supported bilayer ($n = 10$)	diI	uniform	0.37 ± 0.02	0.37 ± 0.02	76
Erythrocyte − BSA ($n = 18$)	diI	nonpunctate, close contact	0.23 ± 0.05	0.23 ± 0.05	93
Erythrocyte + BSA ($n = 6$)	diI	nonpunctate, close contact	0.22 ± 0.03	0.21 ± 0.03	100*
Erythrocyte − BSA ($n = 6$)	diI	punctate	0.31 ± 0.03	0.40 ± 0.06	55
Erythrocyte − BSA ($n = 18$)	diI	cell edge	0.29 ± 0.04	0.36 ± 0.06	62
Erythrocyte + BSA ($n = 6$)	diI	cell edge	0.30 ± 0.03	0.39 ± 0.08	57
Macrophage ($n = 4$)	r-dextran	uniform	1.1 ± 0.2	1.1 ± 0.2	–
Macrophage ($n = 7$)	diI	peripheral zone	0.26 ± 0.03	0.26 ± 0.03	85
Macrophage ($n = 7$)	diI	punctate, central zone	0.50 ± 0.16	0.58 ± 0.2	27
Macrophage ($n = 7$)	diI	central zone	0.31 ± 0.03	0.29 ± 0.03	77

Ratios for both original and deconvoluted images are shown. As expected, deconvoluted images display more variation in *p/s* because the structures appear sharper with less spatial mixing. The expected theoretical values for the *p/s* ratios depend upon the transition dipole directions in the diI molecule and upon the orientational distributions of the diI in the samples, neither of which is known unambiguously. However, a theoretical range of physically possible *p/s* ratios can be given as follows. For diI-labeled supported bilayer membrane, the lower limit would be 0.16 under the assumption that the transition dipoles lie exactly in the plane of a uniform bilayer parallel to the glass substrate in an $n = 1.33$ solution. For r-dextran-loaded macrophages, the range is 0.80 to 1.19, with the lower limit for r-dextran rotationally immobile but isotropic in orientational distribution, and the upper limit for fast isotropic rotational motion. For diI-labeled membranes of erythrocytes and macrophages, the possible range is quite broad: a *p/s* ratio of 0.08 would result for transition dipoles that lie exactly in the plane of a membrane parallel to the glass substrate in an $n = 1.38$ medium; a *p/s* ratio of 0.86 would result from a submicroscopic spherical vesicle in an $n = 1.38$ medium.

*Because the lowest *p/s* ratio observed is 0.21 (for the erythrocyte + BSA sample) rather than the theoretical minimum value of 0.08, we assume the difference can be accounted for by transition dipoles that lie at some nonzero angle with respect to the conjugated bridge of diI (see Appendix A). We then assume that a *p/s* ratio of 0.21 corresponds to a 100% substrate-parallel membrane. Ratios higher than 0.21 then can be interpreted as a percent of membrane assumed to be substrate-parallel with the remainder assumed to be isotropically oriented as in submicroscopic spherical vesicles, as calculated by Eq. 6. (In an alternative view, the *p/s* ratios of 0.36 and 0.39 measured at erythrocyte edges also can be interpreted reasonably as flat membrane oriented at some angle θ in the range 21–28°.)

predictably biconcave with BSA added to the buffer. Several results are notable from the numerical results in Table 3. 1) At nonpunctate areas where the cell is in closest contact to the substrate (the broad ring of the "donut"), the *p/s* ratio (on deconvoluted images) is 0.21 ± 0.03; this is the most ordered (i.e., flattest and most parallel to the substrate) of all the membranes studied. 2) At sparsely distributed speckles in the same general region, the *p/s* ratio increases markedly to ~0.31 ± 0.03, possibly due to blebs or adherent vesicles on the surface of erythrocytes. 3) The *p/s* ratio increases to ~0.39 ± 0.08 as the membrane curves away from the coverslip at the cell periphery (a curve that can also be quantitatively measured as a decrease in evanescent-excited fluorescence intensity). The *p/s* ratio is noisiest near the edge of the cell where the signal is weak and Brownian cell motion is most obvious. 4) The effect of BSA on the *p/s* ratio in the areas of close contact was not statistically significant, although the addition of BSA markedly decreased the number of observed speckles and markedly changed the cells' morphology.

These quantitative results can be seen qualitatively and vividly in images shown in Fig. 7. As expected, the *s*-pol image only slightly shows the location of a putative bleb because geometric foreshortening, which results in extra membrane per pixel, tends to cancel out the reduced fluorescence due to the obliquity of the membrane. However, the *p*-pol image clearly shows this feature, as does the *p/s* ratio image.

Macrophages

R-dextran in the cytoplasm of macrophage cells would be expected to show much less orientational ordering than a membrane probe. Indeed, the high *p/s* ratio of 1.1 in this case (Table 3) is consistent with completely isotropic orientation for r-dextran.

The situation is quite different for macrophages with a diI label in the plasma membrane. Because of the complicated and dynamic morphology of the living macrophage, we first present the images and then the quantitative results. Figure 8 shows *s*-pol, *p*-pol, and *p/s* ratio images for a diI-labeled macrophage cell on a regular acid-treated coverslip. Both the original and the (somewhat crisper) deconvoluted images are depicted. Structures, possibly sites of endocytosis, appear vividly in the *p/s* images that barely appear at all in the *s*-pol image. By comparison, a standard (non-TIR) EPI-illumination image of the same cell shows none of the details of microscopic membrane curvature visible in the TIRF *p/s* image. Ruling out the possibility that the *p/s* features are an artifact of cell motion between successive *s*-pol and *p*-pol exposures (which are alternated with a 6-s time interval), an *s/s* ratio (*upper right panel* of Fig. 8) based on successive *s*-pol exposures (with a 12-s time interval) showed no interesting features.

Two distinctive zones are obvious in TIR images of all macrophages plated on opsonized coverslips and in some macrophages plated on acid treated coverslips: 1) a periph-

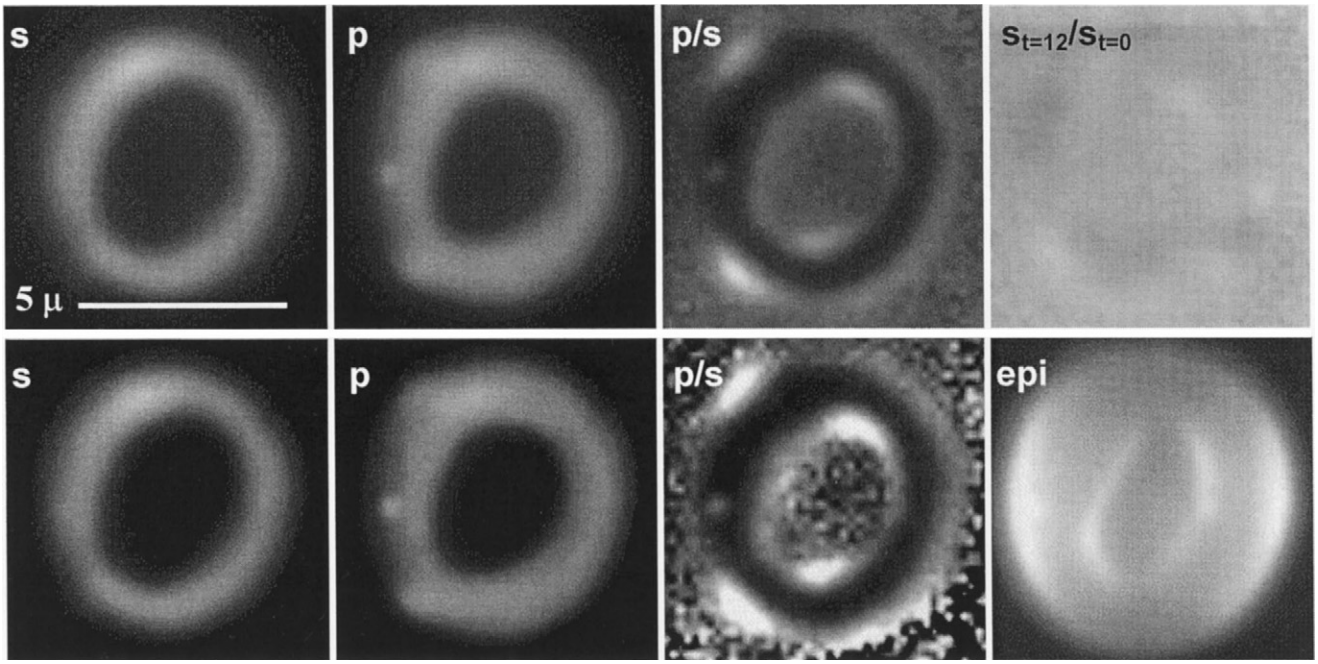

FIGURE 7 Erythrocyte labeled with diI on acid-treated coverslips in the presence of BSA. The first three columns are *s*-pol, *p*-pol, and *p*/*s* ratio images. The top row shows original images; the bottom row shows deconvoluted images. The extreme upper right image is the ratio of two successive *s*-pol images separated in time by 12 s; the relatively featureless field rules out cell motion or imaging artifacts. The extreme lower right image is a standard EPI view. Because the TIR evanescent field drops off exponentially with a characteristic distance shorter than the erythrocyte concavity, the TIR images display the familiar biconcave shape with higher contrast than does the EPI image. The contrast settings for the ratio images are such that black = substrate parallel membrane and white = 50% of membrane in spherical configuration.

eral zone, a ring just inside the periphery of the cell, which has a low *p*/*s* ratio (appears dark in the ratio image) indicating flat and smooth membrane highly parallel to the substrate; and 2) a central zone punctuated with numerous bright speckles in the *p*/*s* ratio, indicating submicroscopic pits and peaks. Macrophages plated on unopsonized coverslips may contain only the central zone. The peripheral zone has previously been found to closely adhere with the coverslip so that macromolecules cannot diffuse beneath the cell (Wright and Silverstein, 1984); whereas the central zone has been found to arch away from the coverslip (Heiple et al., 1990). Table 3 reports three quantitative *p*/*s* ratios: in the peripheral zone, and in the central zone both on and between speckles. The interpretation of the *p*/*s* ratios in terms of fractional orientation (*rightmost column*) confirms that the membrane is much less oriented right at the speckles than between speckles or in the peripheral zone.

In some cases, the *s*-pol image at the location of a speckle (apparent in *p*/*s*) is only mildly brighter, or sometimes dimmer, than neighboring nonspeckle locations. This would be expected if the speckles were ripples, protrusions, or invaginations of existing basal membrane. In other cases, the *s*-pol image at a speckle location is significantly brighter than neighboring nonspeckle locations, suggesting that these particular speckles are distinct vesicles in addition to the existing basal membrane. In either case, it is clear that the peripheral zone is relatively free of ripples, protrusions, invaginations, or vesicles.

To help suggest what the structures corresponding to speckles might be, the quantitative values of the strongly orientation-sensitive *p*/*s* ratios can be examined as a function of the *s*-pol intensity. The brightest speckles in *s*-pol have the highest *p*/*s* ratios (=0.34), which is ~1.3 ± 0.1 ($n = 4$) times greater than neighboring nonspeckle locations. Based on the assumption that the brightest pixels contain fluorescence from the basal membrane (the same at every pixel) plus fluorescence from additional membrane (distinct vesicles, docked vesicles, or membrane invaginations), we subtracted from every pixel the basal membrane fluorescence, as measured from a region of smooth flat membrane, and then took the *p*/*s* ratios of the remaining fluorescence. Figure 9 shows a plot of the correlation between *s*-pol brightness and $\Delta p/\Delta s$ value at the same location, based on pixel data from four cells. As expected for quotients with noisy denominators, the $\Delta p/\Delta s$ ratios shown in Fig. 9 vary greatly for small *s*-pol intensity. The upper dotted line displays the theoretically expected ratio for membrane in submicroscopic spherical vesicle configuration; the lower dotted line displays the expected ratio for substrate-parallel membrane. For the highest *s*-pol intensities, our observed ratios cluster toward a flat value between these two extremes. This suggests that the speckles are either submicroscopic vesicles that are somewhat flattened, or larger vesicles that are only partly immersed in the evanescent field.

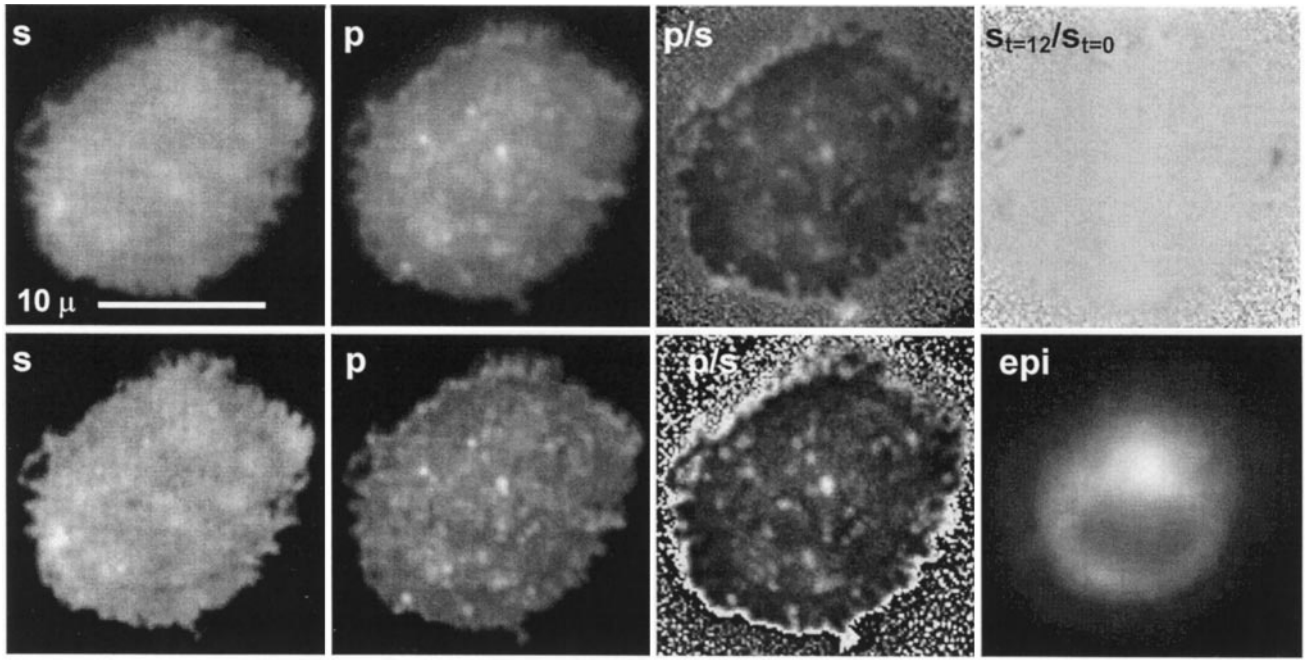

FIGURE 8 Macrophage labeled with diI on acid-treated coverslips. The first three columns are *s*-pol, *p*-pol, and *p*/*s* ratio images. The top row shows original images; the bottom row shows deconvoluted images. The extreme upper right image is the ratio of two successive *s*-pol images separated in time by 12 s; the relatively featureless field rules out cell motion or imaging artifacts. The extreme lower right image is a standard EPI view, focused at the cell/substrate contact plane; blebs and invaginations are much more difficult to see because of out-of-focus fluorescence. The deconvoluted ratio image shows more contrast than the original ratio image at the same display settings. The contrast settings for the ratio images are the same as in Fig. 7.

Opsonization of the coverslip is known to increase the adherence of macrophages, and it might be expected to change the morphology at the cell–substrate contact. Figure 10, showing *s*-pol, *p*-pol, and *p*/*s* ratios for unopsonized versus opsonized substrates, confirms this morphology change. The peripheral zone is much wider in the opsonized (Fig. 10, *d–f*) than in the unopsonized (Fig. 10, *a–c*). The peripheral zone in the opsonized sample is also the flattest part of the membrane: it has a *p*/*s* ratio that is 13 ± 7% (n = 4) lower than the lowest *p*/*s* ratio in the central part of the cell's basal membrane. However, there was no significant ratio difference between peripheral zones of macrophages on opsonized versus acid-treated unopsonized coverslips. These morphologies are consistent with earlier descriptions of macrophages engaging opsonized coverslips, in which a broad, peripheral zone of close adherence surrounds a raised, central region (Heiple et al., 1990), often enriched in containing clathrin-coated pits and vesicles (Takemura et al., 1986).

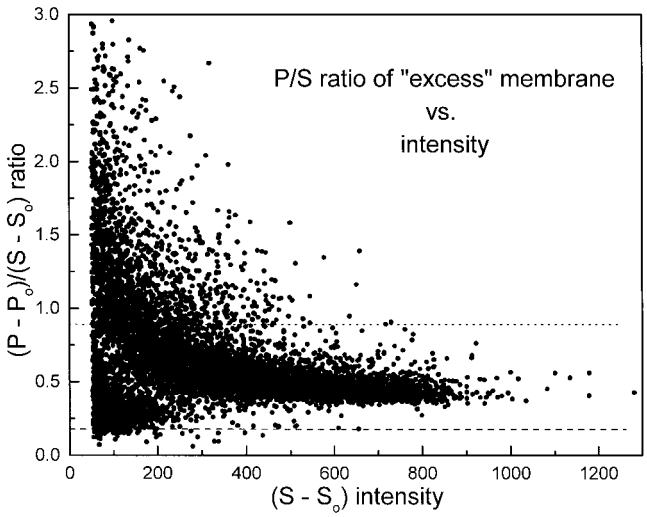

FIGURE 9 Scatter plot of *p*/*s* ratios versus *s*-pol intensity on four diI-labeled macrophages. Each dot represents data at one pixel. The *p*-pol and *s*-pol intensities used for the ratios are actually differences between the full intensities p and s and the intensities p_0 and s_0 observed in substrate-parallel regions, respectively. The dashed lines show the *p*/*s* ratio expected for spherical vesicles (*upper*) and flat substrate-parallel membrane (*lower*). The data are based on deconvoluted images.

Figure 11 shows a time sequence of *p*/*s* images of a macrophage on an unopsonized coverslip with 12-s duration between successive *p*/*s* frames. Speckles and ruffles are seen to be highly dynamic features, appearing and disappearing in time. The dynamics of this region of the macrophage surface have not previously been described. The changing regions of membrane curvature may represent the activities of endocytotic or exocytotic vesicles near the plasma membrane. Macrophages on unopsonized surfaces are reported to contain a paucity of clathrin-coated vesicles, compared to macrophages on opsonized surfaces (Takemura et al., 1986), indicating relatively little endocytotic activity. However, the polarized TIRF images of Fig. 11 indicate that the lower cell surface is more dynamic than it appeared to be in the earlier studies, which relied on elec-

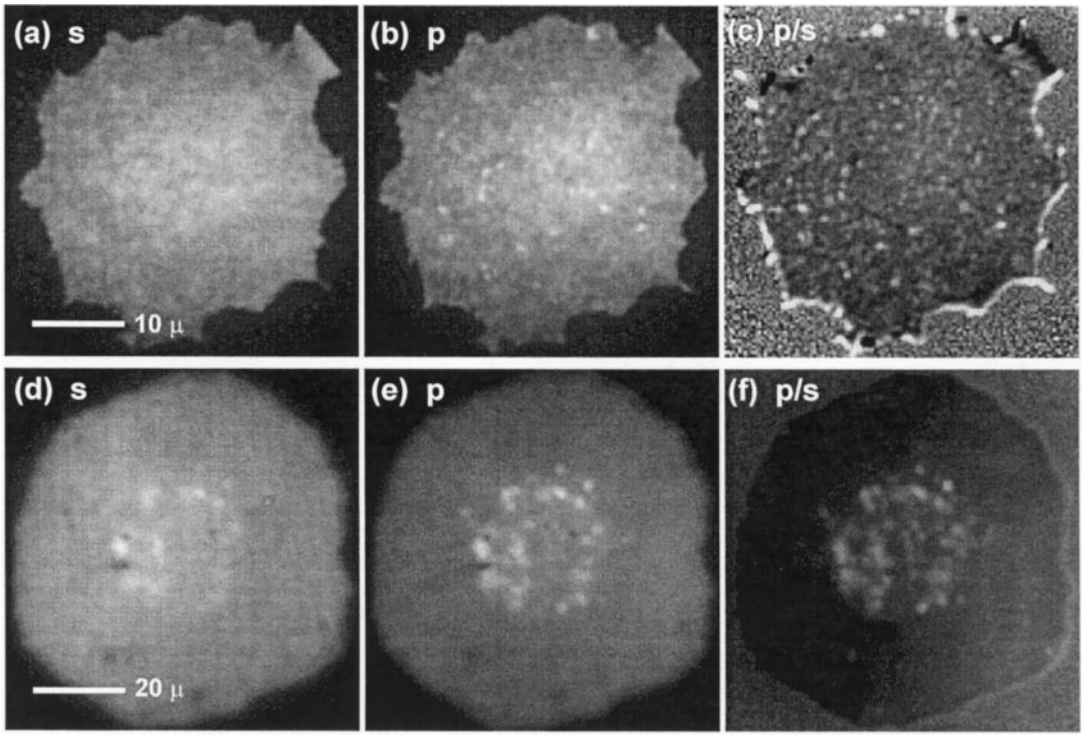

FIGURE 10 Effect of surface opsonization on macrophage morphology. The cell in the top row is on a nonopsonized coverslip. The cell in the bottom row is on an opsonized coverslip, with its much wider circumferential band of speckle-free membrane. The upper images only are deconvoluted. Note the difference in distance scales. The contrast settings for the ratio images are such that black = substrate-parallel membrane and white = 30% of membrane in spherical configuration.

tron microscopy and immunofluorescence microscopy of fixed cells.

DISCUSSION

The polarized TIRF technique introduced here appears to be useful both for qualitative imaging of micromorphological details on cells and for semiquantitative characterization of membrane orientation.

Perhaps of most interest are the spatially resolved *p*/*s* ratios on diI-labeled macrophages. The *p*/*s* ratio images qualitatively highlight structures (possibly vesicles or endocytotic sites) that are far less visible in *s*-pol TIR fluorescence and not visible at all in standard EPI fluorescence. The ratio images also clearly show distinct regions in the macrophages where vesicularization and/or endocytosis occur and do not occur. Membrane curvature at the outer edge of the peripheral zone, where the membrane is presumed to curve away from the substrate, also can be seen. The membrane of the speckle-free peripheral band on opsonized and some unopsonized coverslips was more highly oriented than even the most oriented membrane in the speckle-producing region of the central zone, suggesting that there are differences between the two regions on a submicroscopic scale. Finally, time-lapse *p*/*s* movies show that the structures in the speckle-producing central regions are highly dynamic, appearing and disappearing on time scales of several tens of seconds in cells at 22°C. If image acquisition rates faster than ⅙ Hz were to be used, then it is possible that even more rapid biological events relevant to secretion or endocytosis might be recorded in ratio images. In conjunction with other techniques and possibly specific double-labeling, polarized TIRF may be useful in visualizing a vesicle fusion or budding.

Some erythrocyte images also show speckles of brighter fluorescence, suggesting blebs, vesicles, or vesicle formation. Such spots are often visible only with TIR and not with EPI illumination and have higher *p*/*s* ratios than their immediate surroundings, indicating more membrane curvature at these locations. Membrane very close to the edge of the erythrocyte also has higher *p*/*s* ratios, also indicating obliqueness with the substrate, as expected.

Although some features in macrophages and erythrocytes (such as punctate speckles) often appear as local bright spots in both polarizations (albeit relatively brighter in the *p*-pol image), other features appear dimmer than the immediate surrounding in the *s*-pol image and brighter in the *p*-pol image. Still other features appear dimmer in both images. In any of these cases, more information is obtained regarding membrane orientation from ratio images than in either image separately, because ratio images remove effects due to total amount of membrane present, fluorophore concentration, or fluorophore distance from the coverslip.

In marked contrast to the low *p*/*s* ratios of 0.2 to 0.3 in substrate-parallel regions of diI-labeled membranes, other less oriented samples (such as macrophages scrape-loaded

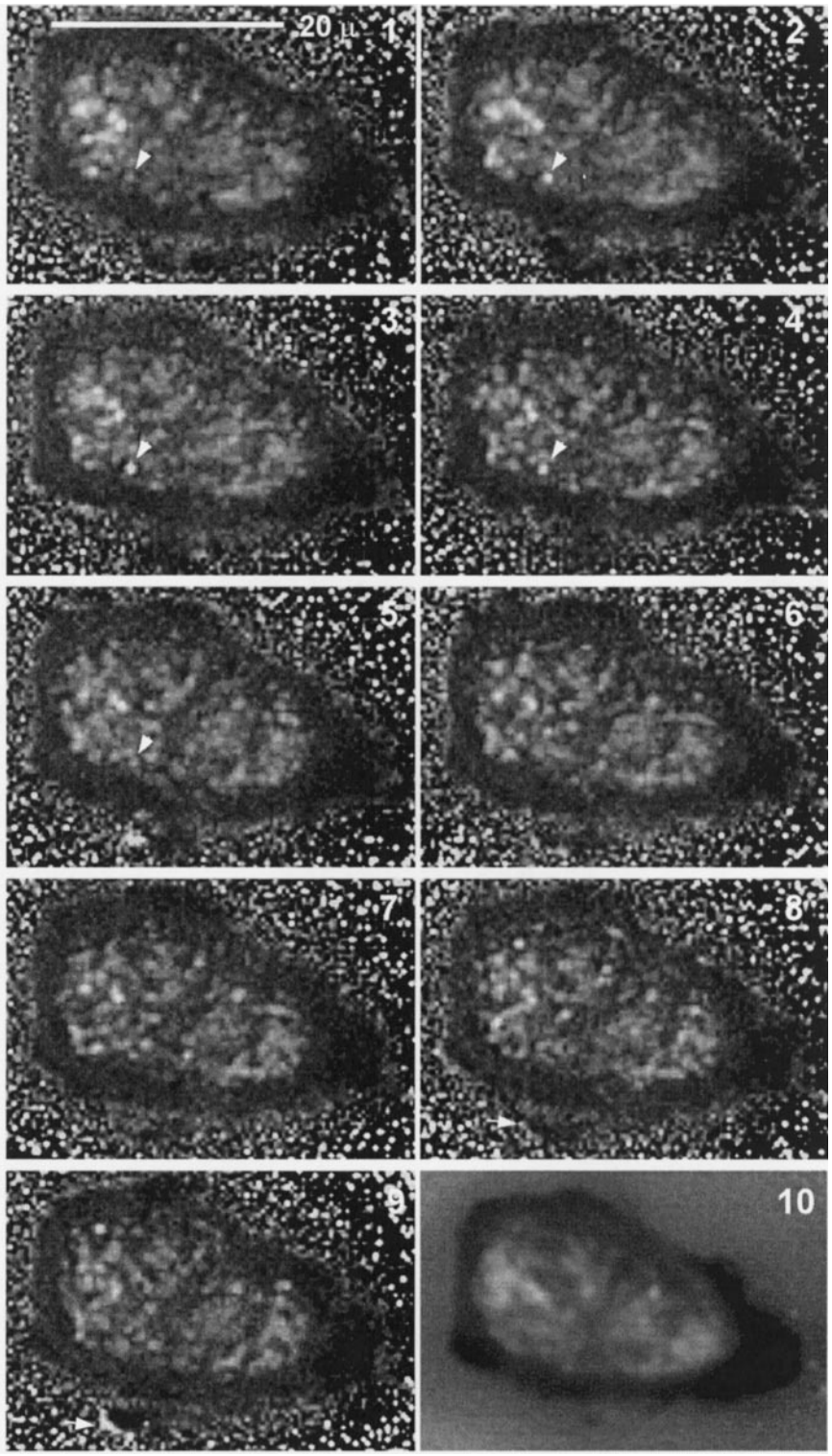

FIGURE 11 (*1–9*) Time sequence of deconvoluted *p*/*s* images of a macrophage on an unopsonized coverslip. The interframe duration is 12 s. One arrow (in frames *1–5*) highlights a particular speckle that appears transiently. Another arrow highlights a typical ruffle displaying highly substrate-parallel membrane that changes its morphology rapidly. It is present in all frames and highlighted by an arrow in frames *8* and *9*. The last frame (*10*) is a *p*/*s* ratio of *p*-pol and *s*-pol images, each averaged over all frames taken in a 15-min period. Of course, the individual speckle events are blurred in the average, but a particularly distinct border is seen between the zones in which putative vesicles and endocytotic events occur and do not occur. The contrast settings for the ratio images are the same as in Fig. 7.

with r-dextran, free solutions of r-dextran, and other fluorescent solutions), display *p*/*s* ratios nearer to unity. The numerical value of the experimental *p*/*s* ratios for samples with known diI orientation distributions agree well with theoretical predictions based on known intramolecular dipole angles for carbocyanines (see Appendix A).

Surprisingly, diI-labeled model phospholipid membranes supported on glass display higher *p*/*s* ratios than the nonspeckle regions of diI-labeled membranes of macrophages and erythrocytes, indicating submicroscopic variability in membrane orientation in the model membranes, which is absent or reduced in the smooth regions of biological membranes. This variability is submicroscopic because the fluorescent images appear smooth by eye with few noticeable features. MacKintosh (1997) discusses several submicroscopic conformational patterns that have been observed in

model membranes, including ripples, saddles, and egg-carton-like shapes. For more information on submicroscopic membrane orientation, two intersecting TIR beams could be used. This would result in evanescent field illumination of 3 linearly independent polarizations, which could disentangle the θ and ϕ angular information. Of the diI samples, the least ordered of all was diI directly absorbed to glass, which showed only ~20% of the diI molecules as ordered in a planar configuration.

This study uses, the first time with TIRF, image enhancement by PSF deconvolution. The procedure is particular simple and fast in TIRF, because the images are strictly 2D with no contribution from out-of-focus planes. By contrast, deconvolution in EPI illumination is a nonlinear and slower iterative process that involves processing data from multiple focal planes using a 3D PSF.

In summary, the polarized TIRF technique introduced here may find future applications in the study of endo- and exocytosis, vesicle fusion, and visualization and quantitative characterization of submicroscopic membrane orientation. In addition, the techniques may also be useful for correction of fluorescence variability due to membrane orientation (for example, to better quantify distances measured by evanescent field exponential intensity decay by correcting for intensity variations due to membrane orientation). TIRF is becoming increasingly popular for observing submicroscopic endo- and exocytosis events and secretory granule motions in the submembrane (Lang et al., 1997; Steyer et al., 1997; Steyer and Almers, 1999; Oheim et al., 1998; Johns et al., 1999). The addition of the polarization feature coupled with the use of oriented membrane probes can potentially provide additional information on the orientational dynamics of those phenomena.

APPENDIX A: Intramolecular angles of carbocyanine dipoles

Two parameters that must be incorporated in the theory are the angles of the diI absorption and emission dipoles with respect to the plane of the membrane in which the diI molecule is embedded. These parameters can be partially specified from measurements of initial anisotropy r_0 in time-resolved polarization studies of carbocyanine dyes as reported in the literature. Tapan et al. (1993) measured r_0 as 0.354 in the carbocyanine dye diO-C_2-(5) vesicles, and Cabrini and Verkman (1986) measured r_0 as 0.36 in the carbocyanine dye diS-C_3-(5) incorporated into renal brush border vesicles. Because the carbocyanine molecule has mirror symmetry (where the hydrocarbon tail groups are parallel to the axis of symmetry halfway between them, and the conjugated bridge in the head group is perpendicular to the axis of symmetry), the absorption and emission dipoles angles must exist in symmetrical pairs with respect to the conjugated bridge axis. A numerical calculation can determine the range of allowed angle pairs of the absorption and emission dipoles. To result in an r_0 of 0.36, the larger angle pair (which could be assigned to either the absorption or emission dipoles) ranges from $\{+16°$ and $-16°\}$ to $\{+11°$ and $-11°\}$ and the smaller dipole angle pair ranges from $\{0°\}$ to $\{+11°$ and $-11°\}$, all measured with respect to the conjugated bridge axis. As the magnitude of one angle pair increases, the magnitude of the other angle pair decreases. For example, the dipole pairs could be at $\pm16°$ and 0°, or $\pm13°$ and $\pm9°$, or at $\pm11°$ and $\pm11°$.

As shown in Table 3, diI-labeled erythrocytes gave the lowest *p*/*s* ratio of all the samples observed. For the purpose of inferring definite dipole angles from *p*/*s* ratios, we thereby provisionally assume that the erythrocyte membrane (in the substrate contact region) is 100% uniformly parallel to the substrate, and all the diI molecules embedded in it are perfectly aligned with their axes of symmetry normal to the membrane. The observed deconvoluted *p*/*s* ratio (0.21 ± 0.03) sets the diI absorption angles with respect to the plane of the membrane at $\pm13.5° \pm 1.5°$. Then the known initial anisotropy r_0 for similar carbocyanines demands that the emission dipoles orient at $\pm10°$ with respect to the plane of the membrane. Conversion of these angles to the system used in the body of this paper (i.e., measured with respect to the membrane normal) gives $\theta'_a = 76.5°$ and 103.5° and $\theta'_e = 80°$ and 100°.

APPENDIX B: Orientation of a membrane-relative dipole expressed in Cartesian coordinates

The purpose of this section is to find the Cartesian coordinates of a dipole $\boldsymbol{\mu}$ that has a specific orientation with respect to a locally flat membrane, and that, itself, has specific orientation with respect to the laboratory frame. As shown in Fig. 3, $\boldsymbol{\mu}$ has polar coordinates (θ', ϕ') with respect to the primed membrane axes, and so $\boldsymbol{\mu}$ expressed in primed coordinates is

$$\begin{pmatrix} \mu_{x'} \\ \mu_{y'} \\ \mu_{z'} \end{pmatrix} = \begin{pmatrix} \sin\theta' \cos\phi' \\ \sin\theta' \sin\phi' \\ \cos\theta' \end{pmatrix}. \tag{B1}$$

The membrane orientation (θ, ϕ) represents the polar coordinates of a vector normal to the membrane. The rotation matrix $\mathbf{R}$ from the lab to the membrane system is a product of matrices representing a rotation of ϕ around the z axis followed by a rotation of θ around the new y axis, and so $\boldsymbol{\mu}$ can be expressed with components in the lab frame by use of the inverse rotation matrix $\mathbf{R}^{-1}$,

$$\boldsymbol{\mu} = \begin{pmatrix} \mu_x \\ \mu_y \\ \mu_z \end{pmatrix} = \begin{pmatrix} \cos\theta\cos\phi & -\sin\phi & \sin\theta\cos\phi \\ \cos\theta\sin\phi & \cos\phi & \sin\theta\sin\phi \\ -\sin\theta & 0 & \cos\theta \end{pmatrix} \begin{pmatrix} \sin\theta'\cos\phi' \\ \sin\theta'\sin\phi \\ \cos\theta' \end{pmatrix}, \tag{B2}$$

which gives Eq. 1 of the text.

APPENDIX C: Observed fluorescence from a dipole near an interface by a microscope objective

Eq. (40) of Hellen and Axelrod (1987) is used to calculate the normalized observed intensity S at a particular observation angle from a dipole at $\mathbf{r}'$,

$$S(\mathbf{r}, \mathbf{r}') = \frac{c\sqrt{\epsilon_i}}{8\pi} \frac{\mathcal{A}}{\cos^2\theta' P_T^{\perp}(z') + \sin^2\theta' P_T^{\parallel}(z')} \tag{C1}$$

where

$$\mathcal{A} = \cos^2\theta' |\mathbf{E}^{\mu_z}|^2 + \sin^2\theta' [\cos^2(\phi - \phi') |\mathbf{E}^{\mu_p}|^2 + \sin^2(\phi - \phi') |\mathbf{E}^{\mu_s}|^2] + \cos(\phi - \phi') \cdot (\text{cross-terms}).$$

In Eq. C1, the primed/unprimed notation follows that of Hellen and Axelrod (1987) and is different from that in the body of the present paper: the primed coordinates in Eq. C1 represent the dipole position and orientation at (z', θ', ϕ') and the unprimed coordinates represent the observation

location at (r, θ, ϕ). The denominator of S represents the near-field correction due to the dipole's proximity to the water-glass interface: the evanescent near field of the fluorophore is converted to propagating light in the substrate in a manner that depends on fluorophore orientation and position (Ford and Weber, 1984; Hellen and Axelrod, 1987). The closer the dipole is to the surface, the more of the energy contained in the fluorophore's near field is captured by the glass and converted into propagating light at angles greater than the critical angle for total internal reflection, thereby leaving less energy available to be captured by objectives that gather only subcritical angle light. $P^{\perp,\parallel}$ is the total power emitted by a constant-amplitude dipole oriented normal or parallel to the substrate, respectively; these can be calculated with numerical and residue integration using Eq. (38) of Hellen and Axelrod (1987). The electric field terms E^{μ_z,μ_p,μ_s} in Eq. C1 each represent the electric fields from a dipole oriented along each of the three axes defined with respect to the observation location and the surface. The equations for the electric field are given in Eq. 35b–37b of Hellen and Axelrod (1987) as,

$$|E^{\mu_z}|^2 = \gamma \frac{t_p^2 \sin^2\theta \cos^2\theta}{\epsilon_1 r^2 (1 - (\epsilon_3/\epsilon_1)\sin^2\theta)},$$

$$|E^{\mu_p}|^2 = \gamma \frac{t_p^2 \cos^2\theta}{\epsilon_3 r^2}, \qquad \text{(C2)}$$

$$|E^{\mu_s}|^2 = \gamma \frac{t_s^2 \cos^2\theta}{\epsilon_3 r^2 (1 - (\epsilon_3/\epsilon_1)\sin^2\theta)},$$

where α is a common factor and t_s and t_p represent the products of individual (because the interfaces are separated by more than the coherence length of fluorescence) Fresnel transmission coefficients through the layered water-glass and glass-water interfaces, which depend on θ and the indices of refraction. The fraction of total emitted intensity that is collected by the objective is then

$$a = \int_{\theta=0}^{\sigma} \int_{\phi} S r^2 \sin\theta \, d\phi \, d\theta, \qquad \text{(C3)}$$

where $\sigma = \sin^{-1}(A/n)$, n is the index of refraction of the medium containing the dipole, and A is the numerical aperture of the objective. Because the ϕ integration is performed over $(0, 2\pi)$, the cross terms in S do not contribute.

To determine if it is necessary take the fluorophore near field into account as above, we calculated the fraction α_0 of the total fluorescence emitted by an excited dipole assumed to be far from an interface that can be captured by an objective of numerical aperture A,

$$\alpha_0 = \left(\frac{3}{4}\right)(1-\cos\sigma) - \left(\frac{3}{8}\right)\sin^2\beta[1-\cos\sigma-(1-\cos^3\sigma)/3] - \frac{1}{4}\cos^2\beta(1-\cos^3\sigma), \qquad \text{(C4)}$$

where β is the angle between the emission dipole and the z axis. Eq. C4 assumes no reflective losses at any interface and no near-field effects. We found that this far field-only theory results in an α_0 that is ~30% different than the full theory α at $z' = 1$ nm, and less than 2% different for z' greater than ~80 nm. A good approximation was found to be

$$\alpha_1 = \alpha_0 + 0.24e^{-z'/50\text{nm}}. \qquad \text{(C5)}$$

This approximation produces an α_1 that agrees with the full theory to within less than a 1% difference for our particular objective. Fig. C1 shows both α for the full theory as a function of the dipole's orientation and distance from the substrate z', and α_0 for comparison.

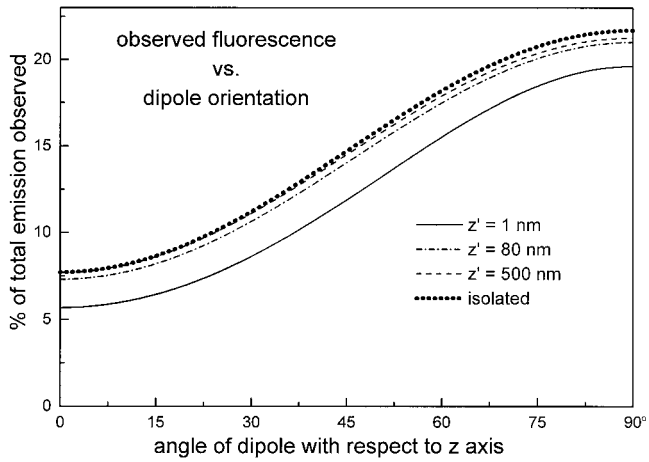

FIGURE C1 The power P_2 of light emitted by an oriented dipole (in $n = 1.33$ solution) at several distances z' from a glass ($n = 1.52$) substrate, propagated through the substrate, and then collected by a 1.0 NA water objective, as a function of the angle between μ and the z axis. P_2 here is expressed as a percentage relative to the total amount of light that would have been emitted by a isolated dipole (in the absence of an interface). If μ is normalized as a unit vector, the cosine of angle shown as the abscissa is simply μ_z, which is a function of θ, θ', and ϕ' as shown in Eq. 1. For numerical calculations with these curves, a third-order polynomial was fit to discrete values of P_2 versus angle.

We thank Rhonda Dzakpasu for the preparation of model membranes, Albert W. Tsang and Kirsten Oesgergaard for macrophage cell culturing, and Alan Kulawik for discussions on image deconvolution. Supported by National Institutes of Health GM08270 and AI 35950 (J.S.), National Institutes of Health 1R01 NS38129 (D.A.) and National Science Foundation MCB 9405928 (D.A.).

REFERENCES

Axelrod, D. 1979. Carbocyanine dye orientation in red cell membrane studied by microscopic fluorescence polarization. *Biophys. J.* 26: 557–574.

Axelrod, D., E. H. Hellen, and R. M. Fulbright. 1992. Total internal reflection fluorescence. *In* Topics in Fluorescence Spectroscopy, Vol. 3, J. R. Lakowicz, editor. Plenum Press, New York. (Note that this reference has two misprints: the phase factor of Eq. 7.6 should be $\exp(-i\delta_p)$, and the denominator of Eq. 7.4 should be a square-root.)

Bradley, R. A., W. G. Martin, and H. Schneider. 1973. Dynamic behavior of fluorescent probes in lipid bilayer model membranes. *Biochemistry.* 12:268–275.

Cabrini, G., and A. S. Verkman. 1986. Mechanism of interaction of the cyanine dye DiS-C_3-(5) with renal brush-border vesicles. *J. Membrane Biol.* 90:163–175.

Das T., N. Periasamy, and G. Krishnamoorthy. 1993. Mechanism of response of potential-sensitive dyes studied by time resolved fluorescence. *Biophys. J.* 64:1122–1132.

Dickson, R. M., D. J. Norris, and W. E. Moerner. 1998. Simultaneous imaging of individual molecules aligned both parallel and perpendicular to the optic axis. *Phys. Rev. Lett.* 81:5322–5325.

Ford, G. W., and W. H. Weber. 1984. Electromagnetic interactions of molecules with metal surfaces. *Phys. Rep.* 113:195–287.

Heiple, J. M., S. D. Wright, N. S. Allen, and S. C. Silverstein. 1990. Macrophages form circular zones of very close apposition to IgG-coated surfaces. *Cell Motil. Cytoskel.* 15:260–270.

Hellen, E. H., and D. Axelrod, 1987. Fluorescence emission at dielectric and metal-film interfaces. *J. Opt. Soc. Am. B.* 4:337–350.

Hellen, E. H., R. M. Fulbright, and D. Axelrod. 1988. Total internal reflection fluorescence: theory and applications at biosurfaces. *In* Spectroscopic Membrane Probes, L. Loew, editor. CRC Press, Boca Raton, FL. 47–79.

Hollenbeck, P. J., and J. A. Swanson. 1990. Radial extension of macrophage tubular lysosomes supported by kinesin. *Nature.* 346:864–866.

Johns, L. M., E. A. Shelden, E. S. Levitan, R. W. Holz, and D. Axelrod. 1999. Motion of chromaffin granules near the plasma membrane as visualized with total internal reflection fluorescence microscopy. *Biophys. J.* 76:A70.

Lang, T., I. Wacker, J. Steyer, C. Kaether, I. Wunderlich, T. Soldati, H.-H. Gerdes, W. Almers. 1997. Ca^{2+}-triggered peptide secretion in single cells imaged with green fluorescent protein and evanescent-wave microscopy. *Neuron.* 18:857–863.

Mc Kiernan, A. M., R. I. MacDonald, R. M. MacDonald, and D. Axelrod. 1997. Cytoskeletal protein binding kinetics at planar phospholipid membranes. *Biophys. J.* 73:1987–1998.

MacKintosh, F. C. 1997. Internal structures in membranes: ripples, hats, saddles, and egg cartons. *Curr. Opin. Colloid Interface Sci.* 2:382.

McNeil, P. L., R. F. Murphy, F. Lanni, and D. L. Taylor. 1984. A method for incorporating macromolecules into adherent cells. *J. Cell Biol.* 98: 1556–1564.

Oheim, M., D. Loerke, W. Stuhmer, and R. H. Chow. 1998. The last few milliseconds in the life of a secretory granule. Docking, dynamics and fusion visualized by total internal reflection fluorescence microscopy (TIRFM). *Eur. Biophys. J.* 27:83–98.

Shaw, W. T., and J. Tigg. 1994. Applied Mathematica. Addison-Wesley Publishing Co., Reading, MA. 419–423.

Steyer, J. A., and Almers, W. 1999. Tracking single secretory granules in live chromaffin cells by evanescent-field fluorescence microscopy. *Biophys. J.* 76:2262–2271.

Steyer, J. A., H. Horstmann, and W. Almers. 1997. Transport, docking and exocytosis of single secretory granules in live chromaffin cells. *Nature.* 388:474–478.

Stout, A. L., and D. Axelrod. 1989. Evanescent field excitation of fluorescence by EPI-illumination microscopy. *Appl. Opt.* 28:5237–5242.

Swanson, J. A. 1989. Phorbol esters stimulate macropinocytosis and solute flow through macrophages. *J. Cell Sci.* 94:135–142.

Swanson, J. A., A. Locke, P. Ansel, and P. J. Hollenbeck. 1992. Radial movement of lysosomes along microtubules in permeabilized macrophages. *J. Cell Sci.* 103:201–209.

Takemura, R., P. E. Stenberg, D. F. Bainton, and Z. Werb. 1986. Rapid redistribution of clathrin onto macrophage plasma membranes in response to Fc-receptor-ligand interaction during frustrated phagocytosis. *J. Cell Biol.* 102:55–69.

Velez, M., and D. Axelrod. 1988. Polarized fluorescence photobleaching recovery for measuring rotational diffusion in solutions and membranes. *Biophys. J.* 53:575–591.

Wright, S. D., and S. C. Silverstein. 1984. Phagocytosing macrophages exclude proteins from the zones of contact with opsonized targets. *Nature.* 309:359–361.